Three component SQUID based system for Airborne Natural Field Electromagnetics

Hugo Larnier*, and Glenn Chubak (Dias Geophysical), Michael Schneider (Supracon AG), Markus Schiffler and Ronny Stolz (Leibniz IPHT)

Summary

Natural source electromagnetic surveys are today routinely performed from airborne platforms but limitations in measured components or bandwidth set margins to exploration depth and resolution. Utilizing new quantum sensor systems with a purpose-built suspension and accompanying motion compensation techniques, the exploration value of these systems can be greatly enhanced. We present a new system utilizing a high-performance SQUID sensor and damping platform along with motion compensation that has performance benefits over existing solutions.

Introduction

In the past years there were a number of advances in science and technology including new sensors, accurate navigation and inertial units (IMU) with high precision positioning via differential GPS (dGPS), innovative platforms, powerful computing hardware and numerical algorithms for modelling and interpretation. These advances have been used for new instrumentation and methods for mineral exploration. In the recent times, airborne electromagnetic (AEM) methods have played an especially important role in metalliferous exploration (Nabighian and Asten, 2002; Zhdanov, 2010; Vallée et al., 2011; Smith, 2014). In this work, we lie our focus on a passive AEM method, namely Audio Frequency MAGnetics (AFMAG, in a frequency range from 1Hz to 10kHz) which was proposed by Ward (1959). This method uses natural Earth magnetic field variations for which conductive anomalies over geologic structures induce a vertical magnetic field component while the horizontal field components are relatively uniform over very large areas. There are today three airborne instruments in the industry (Sattel et al., 2019; Prikhodko et al., 2020) which use this method: ZTEM™ and AirMt™ from GeoTech (Legault, 2012) and MobileMT™ (Kuzmin and Bagrianski, 2018) from Expert Geophysics.

Herein, we introduce a new quantum sensor based instrument which is compact enough to be operated on a damped platform. The first chapter will introduce the sensors, the readout principle, and electronics followed by a description of the platform. After this, the theory for the operation and a case study will be presented. Finally, the paper will be summarized, and conclusions will be drawn on the way forward to improve the instrument performance.

Sensing instrument

Any AFMAG system requires a high-resolution vector magnetic field sensor (magnetometer) which measures all three orthogonal magnetic Earth field components. It will be called a 3D vector magnetometer or 3D-VM herein. The various types of sensors for this purpose are reviewed e.g. in Grosz et al. (2017) or lately Stolz et al. (2021). Fluxgate sensors as 3D-VM were demonstrated by Christensen and Dransfield (2002). However, their sensitivity (white noise floor of $\sim 1\text{pT}/\sqrt{\text{Hz}}$) is not sufficient as well as the bandwidth which is mostly about 1kHz. More often, induction coils measuring the time derivative of a vector component $\partial B_i/\partial x_k$ ($i, k \in x, y, z$), are used. This is the case for the three commercial instruments and recent R&D work and also for semi-airborne AEM methods (Wu et al., 2019; Becken et al., 2020). Depending on their implementation, the coils can be large and heavy, have non-neglectable temperature coefficient, have to be well calibrated to derive the vector components instead of their derivative and have sensitivity which reduces with f^{-2} at low frequencies f which may be disadvantageous e.g. Macnae (2006), Asten and Duncan (2012), Wolfgram and Thomson (2018). Here, so-called B-field coils (e.g. Macnae, 2012) could be an option. However, they show significant low frequency noise and a still too high white noise floor of $> 10\text{fT}/\sqrt{\text{Hz}}$. This is the gap for SQUIDs (Superconducting Quantum Interference Devices) as quantum magnetometers which provide a frequency independent transfer function for their sensitivity and extremely low white noise floor. The theory
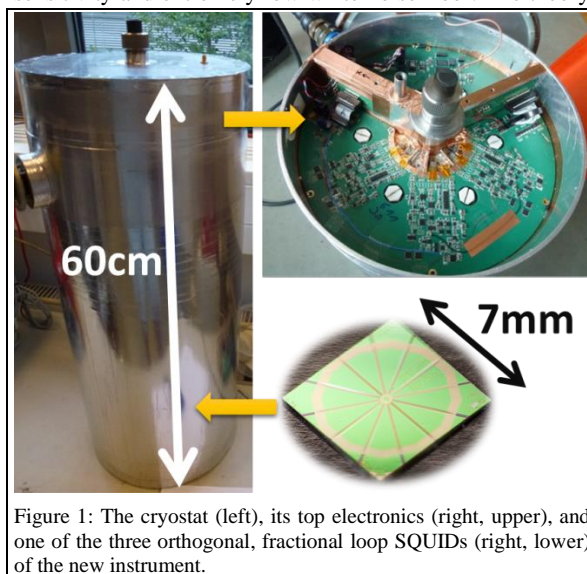

Figure 1: The cryostat (left), its top electronics (right, upper), and one of the three orthogonal, fractional loop SQUIDs (right, lower) of the new instrument.

Three component SQUID based system for Airborne Natural Field Electromagnetics

of SQUIDs and design rules are reviewed e.g. in Clarke and Braginski (2004). The dc SQUIDs, two Josephson junctions intersecting a superconducting loop, used in the 3D-VM are three fractional loop magnetometers (idea of Zimmerman, 1971) with a diameter of 7mm facilitating a sub-µm Josephson junction technology (Schmelz et al., 2011) and a white noise floor of $\sim 0.7\text{fT}/\sqrt{\text{Hz}}$.

In order to overcome the dynamic range limitation of the airborne operation of the 3D-VM, often called signal to noise ratio $SNR = 20 \cdot \log_{10}(B_{max}/B_{noise})$ which is significantly larger than 24bit, a special SQUID readout is used. The periodic SQUID characteristics with a period of a magnetic flux quantum $\Phi_0 = 2.07 \cdot 10^{-15}\text{Vs}$ is linearized using a flux locked loop (FLL, Clarke and Braginski, 2004). This circuit is unlocked and locked with a rate of 1MHz. If the SQUID signals exceed a threshold of $\pm 0.5\Phi_0$, the re-locking process forces the SQUID signal to jump by exactly one Φ_0 towards zero. This jump is detected and given to a counter. The residual SQUID signal in the range of $\pm 0.5\Phi_0$ is digitized using a 18bit analogue to digital converter (ADC). The counter and sub-Φ_0 value of the ADC are merged to provide a hybrid readout of the magnetic field amplitude with $SNR > 32$bit. The data are subsequently decimated down to a 16/32kHz sampling rate. The whole readout process performs in real-time.

The whole instrument called QAMT (Quantum sensor based system for Audiofrequency-MT) consists of a small size data acquisition system (DAS), and a cryostat (cryogen vessel) with 25cm diameter and 60cm height which contains about 8 liters of liquid helium (LHe). This is sufficient for a full week of operation. The cryogenic operation is the only disadvantage of this instrument. However, the low evaporation rate of the LHe reduces the helium costs to a negligible level compared to helicopter operation costs. On top of the cryostat is the full set of electronics with all controls of system operation as shown in figure 1. The cryostat operation is controlled via LAN network from a DAS which contains the batteries with > 10 hours operation and power supply, the controller and memory for data storage, a dGPS and interfaces for the IMU and radar/laser altimeters. The whole instrument weighs ~32kg and can be controlled via WLAN interface or can be operated self-sufficiently.

For the ground station, another SQUID based 3D-VM instrument (Chwala et al., 2013) is used with an electrode array for recording of the horizontal electric field components. A GPS base for post-processing of the mobile dGPS data is also included.

Instrument platform

The reduction of motion noise is the main challenge for all AEM instruments which make use of vector type magnetometers. For the QAMT instrument, it is implemented on two parallel tracks: the post-processing using dGPS
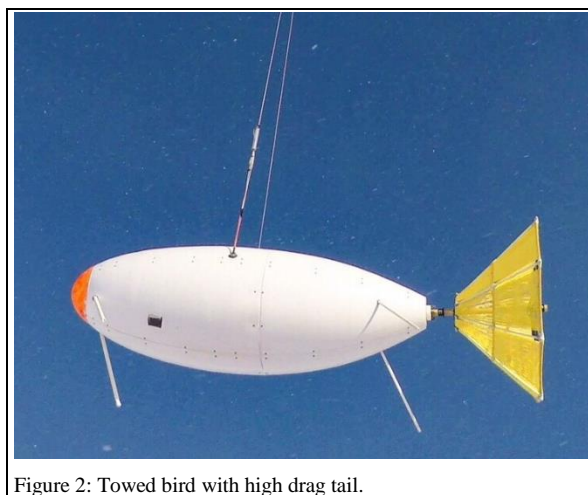

Figure 2: Towed bird with high drag tail.

and IMU data reduces the motion noise below ~20Hz and by the towed bird and suspension for frequencies > 5Hz.

The cryostat with sensors is placed inside the bird on an inner platform. It has a mechanical isolation system which is designed to limit the transfer of high frequency motion between the outer and inner structures. The motion compensation system is far more effective with low frequency rotations and translations, so the primary function of the suspension is to simply transfer high frequency motion into low frequency motion. The absolute energy of the transferred motion is not significantly attenuated.

The effect of the damped and isolated internal platform is clearly observed in the exemplary motion noise spectra, namely the accelerations in vertical direction and the angular rates around the vertical axis (heading) in Figure 3. There is a comparison to a towed bird without isolation and damping drawn. The corner frequency of the platform is ~5Hz. Above this corner, the amplitudes of the rotations and vibrations are significantly decreased. Above ~20Hz
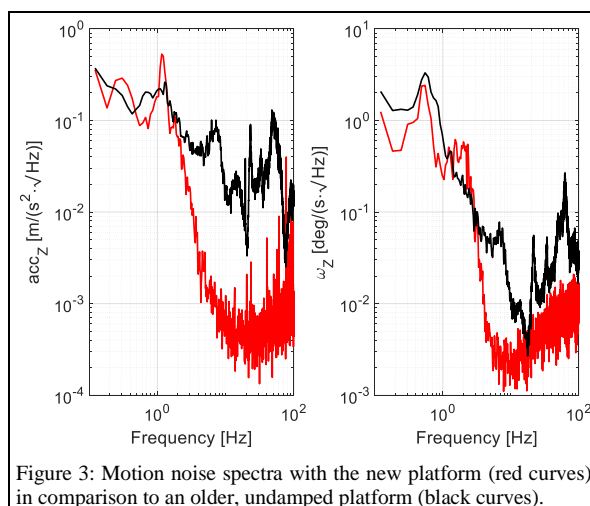

Figure 3: Motion noise spectra with the new platform (red curves) in comparison to an older, undamped platform (black curves).

Three component SQUID based system for Airborne Natural Field Electromagnetics

the resolution of the IMU limits the evaluation of the isolation/damping platform assessment. In the future, we intend to implement an IMU with low magnetic disturbances and improved performance.

Theory of operation

The AFMAG source fields in the frequency range ($1Hz - 10kHz$) are considered originating from lightning storms at large distances and electromagnetic (EM) waves in the area of interest are considered quasi-uniform (Chave and Jones, 2012). Such waves induce eddy currents in the ground that are being measured with electric dipoles at the ground surface. Due to the transient nature of the electric field, they also create a secondary magnetic field, which superposes on the primary. Starting from Maxwell's equations and using the source properties, we then obtain the following equations, which are the foundations of MT (Cantwell, 1960; Rokityansky, 1961):

$$\begin{cases} E_x(\omega) = Z_{xx}(\omega)H_x(\omega) + Z_{xy}(\omega)H_y(\omega) \\ E_y(\omega) = Z_{yx}(\omega)H_x(\omega) + Z_{yy}(\omega)H_y(\omega) \\ H_z(\omega) = T_x(\omega)H_x(\omega) + T_y(\omega)H_y(\omega) \end{cases} \quad (1)$$

where E is the electric field (mV/km), H the magnetic field (nT). Z and T are respectively the impedance tensor and the tipper function. Both are directly related to the geometry of the resistivity distribution in the ground.

In equation (1), all fields are measured on the ground. For the QAMT system, all magnetic field components are measured on the system that is being flown over a specified survey area, and we therefore obtain:

$$\begin{cases} E_{x,b}(\omega) = Z_{xx}(\omega)H_{x,m}(\omega) + Z_{xy}(\omega)H_{y,m}(\omega) \\ E_{y,b}(\omega) = Z_{yx}(\omega)H_{x,m}(\omega) + Z_{yy}(\omega)H_{y,m}(\omega) \\ H_{z,m}(\omega) = T_x(\omega)H_{x,m}(\omega) + T_y(\omega)H_{y,m}(\omega) \end{cases} \quad (2)$$

where the subscript m indicates mobile components. Electric fields are measured at a base station located near the survey area and are thus indicated with a subscript b.

As already pointed out, three commercially available systems follow the same methodology. However, they differ in the data measured in the air and on the ground, the geometry, and the frequency range and thus in their sensitivities to sub-surface conductivity structures (Sattel et al., 2019).

The ZTEM™ system only measures the mobile vertical field at a sampling rate of 2kHz (Legault, 2012), and uses horizontal magnetic field at a remote base station:

$$H_z(\omega) = H_{x,b}(\omega)T_{x,b}(\omega) + H_{y,b}(\omega)T_{y,b}(\omega) \quad (3)$$

where the subscript b indicates fields measured at the base station. While most of the geological information is contained in the vertical component of the magnetic field, the horizontal components also contain the secondary term

related to the transient nature of the induced eddy currents and therefore contribute to the sensitivity of the Tipper function.

The AirMT system, introduced by Geotech in 2010 measures all three components of the magnetic vector, but at a sampling rate of 2kHz, limiting the exploration at shallow depths.

Finally, the MobileMT system uses, so far, only the mobile horizontal magnetic field (Sattel et al., 2019), including the secondary sources related to the geology, but does not use the vertical magnetic field and therefore cannot determine the tipper. As stated in the same study by Sattel et al., (2019) the response range for such system design is very small, and therefore relies on the capability of being able to measure the low signal-to-noise ratio secondary magnetic field related to local resistivity geometry. However, the bandwidth has been extended to include frequencies up to 20kHz allowing for the characterization of shallow sources. The newly introduced QAMT system allows the accurate measurement of all three components of the Earth magnetic field during data acquisition, allowing for the determination of the full Tipper described equation (1), as well as the impedance tensor with electric fields at the base station, with an expected bandwidth from 10Hz up to 10kHz. The lower range of this bandwidth being related to a change in the geomagnetic source mechanism.

Data preparation and processing

Compared to ground MT where sensors are properly dug in the ground to avoid any movement and carefully oriented in a proper reference frame, preparation of QAMT data first requires time series synchronization (airborne and ground-based system signals), flux jump removal (Schönau et al., 2013), magnetometer calibration (Schiffler et al., 2014), compensation of the rotational effects occurring from the sensor movements during acquisition. This process transforms the acquired time series from a body reference frame to a geocentric or geomagnetic reference frame, cf. Figure 4.

By using the IMU sensors (accelerometers, gyroscopes), as well as GPS receivers and a fluxgate magnetometer, the calculation of rotation angles (so-called Euler angles or
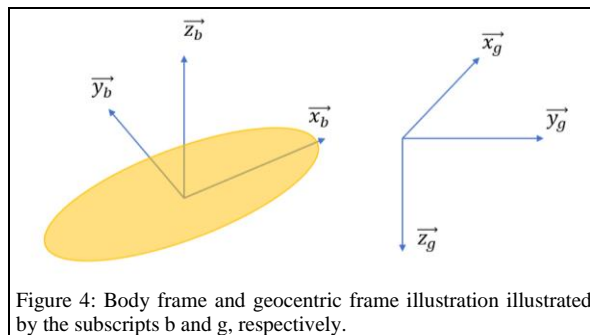

Figure 4: Body frame and geocentric frame illustration illustrated by the subscripts b and g, respectively.

Three component SQUID based system for Airborne Natural Field Electromagnetics

representation in quaternions) is done. The processing of the IMU data starts with the calibration of the sensors and is followed by solving the physical motion or navigation equations using the AINS™ toolbox Kálmán filtering techniques (Shin and El-Sheimy, 2004) which results in an accuracy of the Euler angles of $\sim 0.016°_{rms}$.

The resulting time series, in the geocentric reference frame, are then used in an MT processing framework. The aim of this step is to homogeneously sample the frequency band-width of the system and determine the response function described at (2) for each sampled discrete frequency.

We first perform an automatic detection of atmospherics events to pre-filter time series and only use segments where the signal-to-noise ratio is high enough for data processing (Larnier et al., 2018). We follow state-of-the-art power spectrum density (PSD) estimation and response functions estimations techniques as described in Thomson (1982) and Chave and Thomson (2004) to accurately determine the transfer functions. To do so, we follow a maximum likelihood methodology through an iterative least-squares regression (IRLS). Leverage data is considered and mitigated through the hat matrix by reducing the influence of data points in the predictor variable through another set of leverage weights.

It is important to mention that, as for any statistical metho-dology, there exists a breakdown point where the maximum likelihood will fail if the variability in both predictor and response variables is too high. Therefore, accurate prepara-tion and preprocessing of the data is critical for the determi-nation of the response function. Any deviation from the MT standard model described at equation (2) will contribute to a failure of the robust regression. Such deviations include for example the lack of control on movement or rotation compensation or electronic noise in the system.

Example

The system was flown over the Vredefort impact crater in South Africa (Henkel and Reimold, 2002). This geological structure was previously surveyed with the ZTEM™ system by Geotech (Wade et al., 2019) and therefore offered a good opportunity for comparison.

The survey occurred over the course of three days, on the 21st, 24th, and 25th of February 2020. The ground magnetic field was measured with a SQUID system, and horizontal electric fields were measured in an area where high resisti-vity were expected to increase electric field amplitudes. Nine lines were flown with each line measuring about 70km long with line-to-line distance of 1km. Over the three days, the 21st and the 25th were characterized by significantly lower signal intensity than the 24th.

Figure 5 displays the processed Tipper T_x for a frequency of 122Hz for the lines 103 and 104 surveyed on the 24th. Both lines display coherent features. A clear signature is visible and coherent with geological boundaries of the
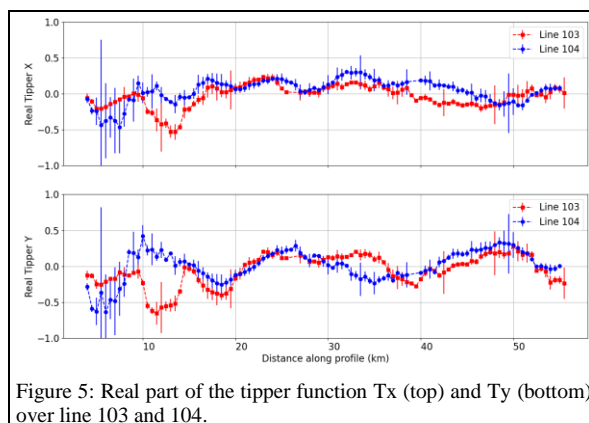

Figure 5: Real part of the tipper function Tx (top) and Ty (bottom) over line 103 and 104.

crater whereas the rest of the line contains little or no tipper signal. Other flight days resulted in very low signal amplitude (25th) and helicopter noise on the 21st so will not be shown here.

During this test flight, we also narrowed down some sources of noise on both the cryostat electronics and the damping platform. Both contributed to the overall noise level that we observed on the time series. The test was nevertheless a success in confirming the validity of the system and assessing all required processing components. The remaining points of contention have been since addressed after this test survey.

Conclusions

A new AFMAG system based on a SQUID sensor and a motion damping platform has been introduced and theore-tical advantages in terms of sensitivity and processing workflow have been discussed.

Field testing has shown great promise in the potential of the QAMT system but also showed where modifications had to be made. Major improvements to the instrument have since been completed and future scheduled test surveys should demonstrate the capabilities of this system.

Acknowledgments

REFERENCES

Asten, M. W., and A. C. Duncan, 2012, The quantitative advantages of using B-field sensors in time-domain EM measurement for mineral exploration and unexploded ordnance search: Geophysics, **77**, no. 4, WB137–WB148, doi: https://doi.org/10.1190/geo2011-0385.1.

Becken, M., C. G. Nittinger, M. Smirnova, A. Steuer, T. Martin, H. Petersen, U. Meyer, W. Mörbe, P. Yogeshwar, B. Tezkan, U. Matzander, B. Friedrichs, R. Rochlitz, T. Günther, M. Schiffler, and R. Stolz, 2020, DESMEX: A novel system development for semi-airborne electromagnetic exploration: Geophysics, **85**, no. 6, E253–E267, doi: https://doi.org/10.1190/geo2019-0336.1.

Cantwell, T., 1960, Detection and analysis of low frequency magnetotelluric signals: PhD thesis, Massachusetts Institute of Technology.

Chave, A. D., and A. G. Jones, 2012, The magnetotelluric method: Cambridge University Press.

Chave, A. D., and D. J. Thomson, 2004, Bounded influence magnetotelluric response function estimation: Geophysical Journal International, **157**, 988–1006, doi: https://doi.org/10.1111/j.1365-246X.2004.02203.x.

Christensen, A. N., and M. H. Dransfield, 2002, Airborne vector magnetometry over banded iron-formations: SEG Technical Program Expanded Abstracts, 13–16, doi: https://doi.org/10.1190/1.1816921.

Chwala, A., J. Kingman, R. Stolz, M. Schmelz, V. Zakosarenko, S. Linzen, F. Bauer, M. Starkloff, M. Meyer, and H. G. Meyer, 2013, Noise characterization of highly sensitive SQUID magnetometer systems in unshielded environments: Superconductor Science & Technology, **26**, 035017, doi: https://doi.org/10.1088/0953-2048/26/3/035017.

Clarke, J., and A. I. Braginski, eds., 2004, The SQUID handbook: Wiley-VCH Verlag GmbH & Co. KGaA.

Grosz, A., M. J. Haji-Sheikh, and S. C. Mukhopadhyay, eds., 2017, High sensitivity magnetometers: Springer International Publishing.

Henkel, H., and W. U. Reimold, 2002, Magnetic model of the central uplift of the Vredefort impact structure, South Africa: Journal of Applied Geophysics, **51**, 43–62, doi: https://doi.org/10.1016/S0926-9851(02)00214-8.

Key, K., 2016, MARE2DEM: A 2-D inversion code for controlled-source electromagnetic and magnetotelluric data: Geophysical Journal International, **207**, 571–588, doi: https://doi.org/10.1093/gji/ggw290.

Kuzmin, P., and A. Bagrianski, 2018, MobileMT: Next Generation of Passive Airborne AFMAG EM Technology.

Larnier, H., P. Sailhac, and A. Chambodut, 2018, Detection and characterization of lightning-based sources using continuous wavelet transform: Application to audio-magnetotellurics: Geophysical Journal International, **212**, 103–118, doi: https://doi.org/10.1093/gji/ggx418.

Legault, J. M., 2012, Ten years of passive airborne AFMAG EM development for mineral exploration: SEG Technical Program Expanded Abstracts, 1–6, doi: https://doi.org/10.1190/segam2012-1267.1.

Macnae, J., 2012, Design and testing of ARMIT magnetic field sensors for EM systems: ASEG Extended Abstracts, **2012**, 1–3, doi: https://doi.org/10.1071/ASEG2012ab343.

Macnae, J. C., 2006, Why bother with B? when you can have dB/dt?: SEG.

Nabighian, M. N., and M. W. Asten, 2002, Metalliferous mining geophysics—State of the art in the last decade of the 20th century and the beginning of the new millennium: Geophysics, **67**, no. 3, 964–978, doi: https://doi.org/10.1190/1.1484538.

Prikhodko, A., P. Kuzmin, and A. Bagrianski, 2020, 60 Years of airborne AFMAG method evolution: OSF, 0–15, doi: https://doi.org/10.17605/OSF.IO/89FKJ.

Rokityansky, I. I., 1961, On application of magnetotelluric method on anisotropic and inhomogenious massifs: Izv. Akad. Nauk SSSR. ser. Geophys., **11**, 1607–1613.

Sattel, D., K. Witherly, and V. Kaminski, 2019, A brief analysis of MobileMT data: SEG Technical Program Expanded Abstracts, 2138–2142, doi: https://doi.org/10.1190/segam2019-3215437.1.

Schiffler, M., M. Queitsch, R. Stolz, A. Chwala, W. Krech, H. G. Meyer, and N. Kukowski, 2014, Calibration of SQUID vector magnetometers in full tensor gradiometry systems: Geophysical Journal International, **198**, 954–964, doi: https://doi.org/10.1093/gji/ggu173.

Schmelz, M., R. Stolz, V. Zakosarenko, T. Schoenau, S. Anders, L. Fritzsch, M. Mueck, and H. G. Meyer, 2011, Field- stable SQUID magnetometer with sub-fT Hz(-1/2) resolution based on sub-micrometer cross-type Josephson tunnel junctions: Superconductor Science & Technology, **24**, 65009, doi: https://doi.org/10.1088/0953-2048/24/6/065009.

Schönau, T., M. Schneider, M. Schiffler, M. Schmelz, R. Stolz, and H. G. Meyer, 2013, Removal of step-edges and corresponding Gibbs ringing in SQUID-based geomagnetic data: Measurement Science and Technology, **24**, 125004, doi: https://doi.org/10.1088/0957-0233/24/12/125004.

Shin, E. H., and N. El-Sheimy, 2004, Aided Inertial Navigation System (AINS™) Toolbox for MatLab\textregistered Software: INS/GPS integration software, Mobile Multi-Sensors Systems (MMSS) research group, the University of Calgary, http://mms.geomatics.ucalgary.ca/Research/research.htm.

Smith, R., 2014, Electromagnetic Induction methods in mining geophysics from 2008 to 2012: Surveys in Geophysics, **35**, 123–156, doi: https://doi.org/10.1007/s10712-013-9227-1.

Stolz, R., M. Schmelz, V. Zakosarenko, C. P. Foley, K. Tanabe, X. Xie, and R. Fagaly, 2021, Superconducting sensors and methods in geophysical applications: Superconductor Science and Technology, **34**, 033001, doi: https://doi.org/10.1088/1361-6668/abd7ce.

Thomson, D. J., 1982, Spectrum estimation and harmonic analysis: Proceedings of the IEEE, **70**, 1055–1096, doi: https://doi.org/10.1109/PROC.1982.12433.

Vallée, M. A., R. S. Smith, and P. Keating, 2011, Metalliferous mining geophysics — State of the art after a decade in the new millennium: Geophysics, **76**, no. 4, W31–W50, doi: https://doi.org/10.1190/1.3587224.

Wade, T., J. M. Legault, G. Plastow, C. Izarra, and A. Bagrianski, 2019, Results of an integrated helicopter ZTEM-gravity-magnetic system test survey over the Vredefort Dome Structure, South Africa: ASEG Extended Abstracts, **2016**, 1–4, doi: https://doi.org/10.1071/ASEG2016ab265.

Ward, S. H., 1959, AFMAG – Airborne and ground: Geophysics, **24**, no. 4, 761–787, doi: https://doi.org/10.1190/1.1438657.

Wolfgram, P., and S. Thomson, 2018, The use of B-field measurements in an airborne time-domain system – Part II: Examples in conductive regimes: Exploration Geophysics, **29**, 225–229, doi: https://doi.org/10.1071/EG998225.

Wu, X., G. Xue, G. Fang, X. Li, and Y. Ji, 2019, The development and applications of the semi-airborne electromagnetic system in China: IEEE Access, **7**, 104956–104966, doi: https://doi.org/10.1109/ACCESS.2019.2930961.

Zhdanov, M. S., 2010, Electromagnetic geophysics: Notes from the past and the road ahead: Geophysics, **75**, no. 5, 75A49–75A66, doi: https://doi.org/10.1190/1.3483901.

Zimmerman, J. E., 1971, Sensitivity enhancement of superconducting quantum interference devices through the use of fractional turn loops: Journal of Applied Physics, **42**, 4483–4487, doi: https://doi.org/10.1063/1.1659798.